systems

MDPI

Article

Surrogate-Based Reconstruction of Structural Damage in Train Collisions: A Systematic Optimization Framework

Hui Zhao [1], Dehong Zhang [2,*] and Ping Xu [3]

[1] Faculty of Maritime and Transportation, Ningbo University, Ningbo 315211, China; zhaohui1@nbu.edu.cn
[2] Guangzhou EMU Depot, China Railway Guangzhou Group Co., Ltd., Guangzhou 511483, China
[3] Key Laboratory for Track Traffic Safety of Ministry of Education, Central South University, Changsha 410075, China
* Correspondence: dehong_zhang_2019@163.com

Abstract

Accurate reconstruction of train collision accidents is essential for understanding impact conditions, assessing crashworthiness, and supporting safety improvements. This study proposes a surrogate-based optimization framework for reconstructing structural damage in train collisions from post-accident observations. The pre-impact kinematic state, expressed by a six-dimensional vector of relative offsets, rotations, and impact velocity, is formulated as an inverse problem in which a Sum of Squared Relative Deviations (SSRD) between measured and simulated residual deformations serves as the objective function. A reduced two-vehicle finite element (FE) model is developed to capture the dominant impact dynamics, an Optimal Latin Hypercube Design is used to sample the parameter space, and a Kriging surrogate model is constructed to approximate the response. A simulated annealing algorithm is applied to search for the global minimum. The framework is demonstrated on a real high-speed rear-end collision of electric multiple units. The Kriging model achieves a coefficient of determination of about 0.85, and the optimized kinematic state yields FE-predicted residual deformations that agree with field measurements at key locations to within about 5%. The results show that the method can efficiently reconstruct physically plausible collision scenarios and provide insight into parameter sensitivity and identifiability for railway safety analysis.

Keywords: train collision; accident reconstruction; inverse analysis; structural damage; finite element modelling; surrogate-based optimization

1. Introduction

Train collision accidents often result in severe casualties and fatalities, accompanied by significant structural damage to vehicles and complex multi-vehicle instability phenomena [1–3]. Figure 1 illustrates several typical train collision accidents that have occurred in recent years. To better learn from these events and improve future safety, it is essential not only to analyze the global consequences, but also to reconstruct the detailed collision process. A reliable reconstruction helps clarify the damage mechanisms, trace the evolution of instability, and ultimately supports the improvement of both active and passive safety measures [4].

Check for updates

Academic Editor: James Cale

Received: 31 December 2025
Revised: 24 January 2026
Accepted: 27 January 2026
Published: 31 January 2026

Copyright: © 2026 by the authors. Licensee MDPI, Basel, Switzerland. This article is an open access article distributed under the terms and conditions of the Creative Commons Attribution (CC BY) license.



(**a**) (**b**) (**c**)

Figure 1. Typical train accidents in recent years: (**a**) 2018, United States; (**b**) 2020, Italy; (**c**) 2023, India.

As schematically shown in Figure 2, the evolution of a train collision can be broadly divided into three phases: pre-collision, collision, and post-collision. In the pre-collision phase, emergency braking may be triggered before physical contact. The collision phase is characterized by a short duration and high impact forces; during this phase, the kinetic energy of the train system rapidly transforms into elastoplastic deformation energy and contact interface work [5–7], potentially leading to derailment or climbing if anti-climbing devices fail [8]. After the main impact, the system enters the post-collision phase, which encompasses subsequent derailment, overturning, or secondary impacts until all kinetic energy is dissipated and the vehicles come to stop.

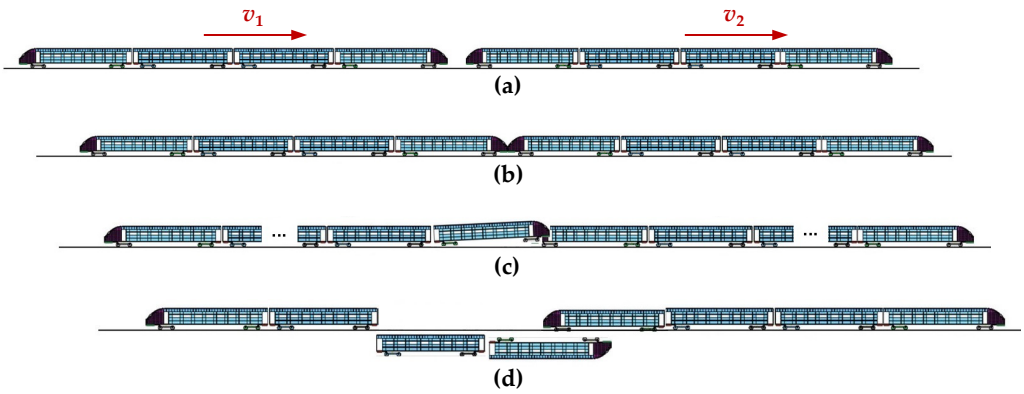


Figure 2. Schematic of the three-phase evolution in train collision accidents: (**a**) Pre-collision deceleration, (**b**) Collision with structural failure, (**c**) Collision with instability behavior, (**d**) Post-collision separation and stop.

The overall evolution of a train collision is therefore extremely complex and highly variable. In practical engineering, a comprehensive numerical analysis of the full process for an entire trainset requires modelling and computational effort much higher than that of conventional crashworthiness simulations. Although there have been attempts to analyze and reconstruct specific rail accidents, systematic methodologies dedicated to train collision reconstruction remain limited. Many existing works focus on reconstructing the scene and identifying causes, but do not deeply address the accurate recovery of the train state before impact and the detailed progression of the accident. For example, Severson [9] developed a three-dimensional multi-body dynamics model for train collisions, predicting the outcomes of full-scale tests involving single- and two- car configurations of traditional North American passenger trains. The model demonstrated high accuracy in simulating longitudinal motion responses but showed significant discrepancies in vertical and lateral motion compared to the test results. Jacobsen [10] utilized Adams software to develop a three-dimensional dynamic model for reconstructing the train collision process from a full-scale impact test conducted in the United States in March 2006. Liu et al. [11] and Shi et al. [12] independently employed a combination of virtual reality and multi-body

dynamics software integrated with PID control techniques to simulate train derailment accidents. These studies advance the understanding of train accident causation by offering methodologies for accident reconstruction and simulation. The United States Department of Transportation and Federal Railroad Administration [13] established a railway accident investigation team to conduct a simplified reconstruction of a Chicago subway commuter train derailment incident. Utilizing on-site investigations and interviews, the team analyzed aspects such as structural deformation, collision dynamics, and passenger casualties. Wei et al. [14] conducted a simulation of an urban rail transit train derailment incident, employing FE analysis to reconstruct the accident model and elucidate the direct causes and processes of vehicle damage within the complex accident scenario. Nevertheless, in most of these contributions, the pre-impact conditions are either assumed to be known or are only described in a qualitative way, and do not tackle the quantitative identification of the full pre-collision kinematic state from post-accident structural damage.

By contrast, the broader field of accident reconstruction has been extensively developed in the context of road traffic collisions [15]. Systematic studies on accident reconstruction began in the 1960s, leading to the development of various techniques for different accident scenarios [16]. Today, road traffic accident reconstruction methods are generally divided into two main types: classical mechanic methods and numerical simulation methods. Classical mechanic methods can be further divided into impulse/momentum methods [17] and energy/deformation methods [18]. These approaches typically operate from a two-dimensional perspective, relying on analytical solutions and empirical formulas for analysis and calculation. Although these methods are efficient, ensuring computational accuracy can be challenging. Numerical simulation methods mainly include multi-body dynamics and FE methods. Multi-body dynamics are favored for their model simplicity and rapid computation, especially in the analysis of human injury in collision accidents [19–21]. However, this method has limitations in representing the elastoplastic deformation characteristics of vehicle structures. In contrast, the FE method can accurately simulate the elastoplastic deformation of vehicle structures and is theoretically considered the most scientific and precise method [22]. Yet, applying detailed FE models directly in accident reconstruction is often restricted by the large number of elements and the associated computational cost.

To reduce simulation iterations and time, various optimization and approximation techniques have been integrated into road accident inverse reconstruction [23–25]. These include, for instance, the use of parallel computing, neural network-based global approximations of FE simulations [26], as well as hybrid frameworks combining momentum methods with multi-body models [27]. Such techniques help to shorten computation time while keeping acceptable accuracy and thus improve the precision of reconstructed pre-accident velocities and other unknown parameters.

Previous studies have provided valuable methods for accident reconstruction, primarily focused on road traffic collisions, where impacts are often modeled as planar events with the primary objective of estimating impact velocities for responsibility analysis. However, unlike road vehicles, the structural configuration of railway vehicles differs fundamentally, resulting in both the distribution of structural damage and the energy transfer pathways during a collision. These differences limit the direct applicability of road-based reconstruction methods to railway collisions. First, unlike road vehicles, a train consists of multiple vehicles, and the collision involves not just the crushing of individual cars but also interactions between adjacent vehicles. This allows impact energy to propagate along the trainset, triggering secondary collisions and often resulting in complex instability modes such as climbing, lateral folding, derailment, or rollover. Second, train car bodies are designed with a stiffness zoning: the non-passenger end zones absorb energy through large plastic

deformations, while the stiffer passenger zones remain mostly elastic to protect occupants. As a result, permanent damage typically concentrates at the car ends. Additionally, train collision investigations may be constrained by incomplete operational data, and residual structural deformation at carbody ends and key joints is typically more accessible. This motivates a damage-based inverse problem, where post-accident deformation is used to infer the unknown pre-impact kinematics. However, two challenges arise: first, high-fidelity finite element models of complete trainsets are complex and difficult to apply systematically, and second, solving the inverse problem with such models is computationally intensive due to the high-dimensional parameter space and the cost of each simulation.

To address these challenges, this paper develops a surrogate-based optimization reconstruction framework for structural damage analysis in train collisions. The optimization reconstruction framework uses post-accident residual deformation to quantitatively identify the unknown pre-impact kinematic state. First, to avoid the prohibitive complexity and computational cost of a full-train FE model, a reduced two-vehicle FE impact model is constructed. Through appropriate simplification and boundary equivalence, the model retains the key structural features and inter-vehicle interactions needed to capture the dominant collision dynamics. Second, to overcome the computational expense of forward simulations and the inefficiency of direct iterative search, a surrogate-based inverse procedure is adopted: an Optimal Latin Hypercube Sampling is used to efficiently cover the six-dimensional pre-impact state parameter space; a Kriging model is then constructed to approximate the damage-related objective function; and simulated annealing is employed to perform global optimization over the resulting response surface, enabling reliable identification of the pre-impact relative state with a limited number of FE evaluations. Together, these steps maintain the physical fidelity required for local structural crushing while significantly reducing expensive FE iterations, achieving a practical balance between computational efficiency and reconstruction accuracy. Finally, the framework is demonstrated on a real high-speed train rear-end collision. The Kriging surrogate shows good predictive performance, and the FE simulation based on the optimized pre-impact state yields residual deformations at key measurement points that agree well with field data. This validates the effectiveness and practical utility of the framework for real-world accident reconstruction.

2. Methodology: Surrogate-Based Inverse Reconstruction Framework

This section introduces a surrogate-based inverse reconstruction framework for train collision analysis. The framework formulates accident reconstruction as a damage-based inverse problem and combines FE modelling, surrogate approximation, and global optimization to achieve computationally efficient parameter identification. Figure 3 provides an overview of the framework, and the main steps and components are described in the following subsections.

2.1. Inverse Problem Formulation

2.1.1. Damage Quantification and Objective Function

Residual structural damage serves as a direct indicator of accident severity and is therefore a key quantity in accident reconstruction. The first step in the reconstruction is to quantify the deviation between numerical predictions and measurements of residual damage.

Let d_{im} denote the measured residual deformation at the i-th damage indicator (e.g., a selected node or section on the vehicle body) and let $d_{is}(\boldsymbol{\theta})$ denote the corresponding deformation predicted by the forward FE model for a given parameter vector $\boldsymbol{\theta}$. To give

equal weight to relative deviations regardless of their absolute magnitude, a Sum of Squared Relative Deviations (SSRD) is adopted as the objective function:

$$\delta(\boldsymbol{\theta}) = \sum_{i=1}^{n} \left(\frac{d_{is}(\boldsymbol{\theta}) - d_{im}}{d_{im}} \right)^2 \tag{1}$$

where n is the total number of selected damage indicators.

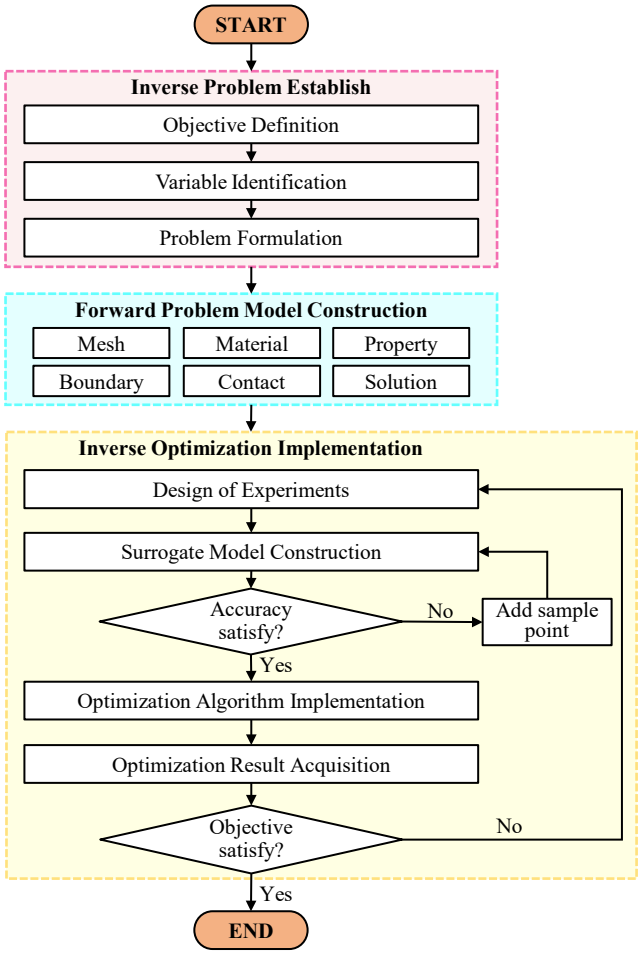


Figure 3. Flowchart of the systematic optimization framework for train collision accident reconstruction.

2.1.2. Kinematic State Variables and Parameterization

Observations from actual train collisions indicate that impacts are rarely perfectly aligned. Vehicle bodies may experience relative offsets and rotations at the moment of collision, which significantly influence the resulting damage morphology.

As illustrated in Figure 4, a right-handed coordinate system is established: the train's direction of travel defines the positive x-axis, the upward direction perpendicular to the track plane as the positive z-axis, and the y-axis is determined by the right-hand rule. The pre-collision state of the train is parameterized by a six-dimensional vector $\boldsymbol{\theta}$, which collects the key kinematic variables governing the impact configuration:

$$\boldsymbol{\theta} = \begin{bmatrix} T_Y & T_Z & R_X & R_Y & R_Z & V \end{bmatrix}^{\mathrm{T}} \tag{2}$$

where T_Y and T_Z denote the lateral and vertical offsets in the vehicle coordinate system; R_X, R_Y, and R_Z are the roll, pitch, and yaw angles about the longitudinal (x), lateral

(y), and vertical (z) axes, respectively; and V is the relative impact velocity along the longitudinal direction.

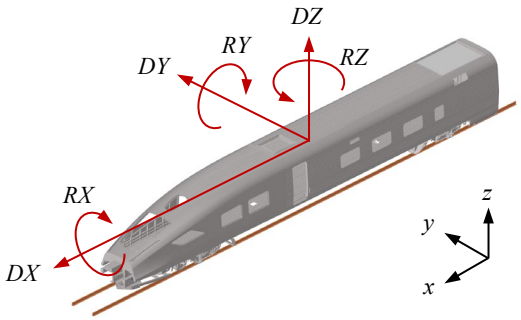


Figure 4. Coordinate system defining the kinematic state parameters of the vehicle.

2.1.3. Mathematical Formulation

The reconstruction problem is formulated as a constrained nonlinear optimization problem. Given the objective function $\delta(\boldsymbol{\theta})$ defined in Equation (1), and lower and upper bounds $\boldsymbol{\theta}^L$ and $\boldsymbol{\theta}^U$ on the parameters $\boldsymbol{\theta}$, the problem can be written as:

$$\begin{aligned} &\underset{\boldsymbol{\theta}}{minimize}\ \ \delta(\boldsymbol{\theta}) \\ &subject\ to\ \boldsymbol{\theta}^L \leq \boldsymbol{\theta} \leq \boldsymbol{\theta}^U \end{aligned} \tag{3}$$

2.2. Forward FE Model

In the proposed inverse reconstruction framework, the forward problem is solved using an explicit nonlinear FE model. The FE model provides a mapping from the pre-impact kinematic parameters to the residual deformation. To make the approach applicable to a broad range of train collision scenarios, a generic FE modelling strategy is adopted, as outlined below.

2.2.1. Geometric Model Simplifications

The two-vehicle collision unit adopted in this study is intended for accident scenarios dominated by local end-structure plastic deformation, where the global vehicle motion remains relatively constrained. The method is not intended for collision scenarios involving pronounced three-dimensional global instabilities, such as derailment, climbing, or rollover.

- Local impact region modeling: Only the two most relevant vehicles (the impacting front of the trailing train and the impacted rear of the leading train) are modelled explicitly, forming a two-vehicle impact unit. The remaining vehicles are represented implicitly through suitable boundary conditions when their influence on the local end-structure response is negligible.
- Structural simplification: For auxiliary underfloor equipment and other non-critical components that do not participate in the crushing deformation, their structural deformation is neglected and only their inertial effect is retained. Accordingly, these items are represented by equivalent lumped masses placed at their actual mounting locations, and the surrounding nodes are rigidly tied to the mass point to transmit inertia forces to the carbody [28]. The primary load-bearing members, such as the carbody shell, underframe, end wall and key reinforcements, are modelled explicitly.
- Bogie and coupler representation: The bogies and couplers are represented by simplified models that reproduce their overall stiffness and mass characteristics without resolving detailed geometry. Their main role in the reconstruction is to transmit loads and constrain relative motion, rather than to provide local damage information.

These simplifications reduce model size and complexity while preserving the main deformation mechanisms at the vehicle ends.

2.2.2. Mesh Density Strategy

Accurate prediction of local plastic deformation and damage requires sufficiently fine meshes in critical regions, whereas coarser meshes may be used in regions with mainly elastic response to reduce computational cost. Therefore, a non-uniform mesh strategy is adopted. Along the carbody length, the structure is divided into several zones according to the expected deformation level. The car ends and collision interface regions, which experience severe crushing and complex folding, are discretized with finer shell elements to resolve local buckling, wrinkling and tearing. The central passenger region, which usually remains elastic or only mildly plastic in longitudinal impacts, is modelled with larger elements. In this way, mesh refinement is concentrated where it is most needed.

2.2.3. Material Model

The primary load-bearing components of modern railway vehicles are thin-walled metallic structures, such as aluminum or steel extrusions and plates. In the present framework, all major structural parts of the carbody are modelled using an elastoplastic constitutive law with failure, so that both plastic deformation and fracture can be reproduced in severe impacts.

A piecewise linear plasticity model is employed to describe the stress–strain behavior under dynamic loading. The basic material parameters are obtained from design data or coupon tests. To account for extensive tearing and local fracture, an effective plastic strain-based failure criterion is introduced. When the accumulated plastic strain in an element exceeds a prescribed failure strain, the element is eroded or its stiffness is reduced.

2.2.4. Boundary and Contact Conditions

Train collisions involve complex contact interactions between deforming structures, and the contact interfaces and contact sequence are not known as a priori. To handle these interactions robustly, an automatic single-surface contact algorithm is used to model both self-contact within a carbody and mutual contact between different vehicles.

Global boundary conditions are imposed according to the accident scenario. Typically, one vehicle is assigned an initial velocity along the longitudinal direction of the track, while the other vehicle is stationary or has a different initial velocity. In some cases, one end of a reference vehicle is constrained to a rigid wall or suitably restrained to represent the constraint effect of the remaining trainset or infrastructure. Symmetrical planes may be used when appropriate to further reduce the model size.

2.2.5. Numerical Solution Procedure

The dynamic response of the FE model is computed using an explicit time integration scheme, which is well suited for highly nonlinear impact problems with complex contact conditions and material failure. For a discretized FE system, the semi-discrete equations of motion time t are:

$$\boldsymbol{M}\ddot{\boldsymbol{u}}(t) = \boldsymbol{F}_{ext}(t) - \boldsymbol{F}_{\text{int}}(\boldsymbol{u}(t),\ \dot{\boldsymbol{u}}(t)) \tag{4}$$

where $\boldsymbol{M}$ is the consistent mass matrix, and $\boldsymbol{u}(t)$, $\dot{\boldsymbol{u}}(t)$ and $\ddot{\boldsymbol{u}}(t)$ are the nodal displacement, velocity, and acceleration vectors, respectively. The internal force vector $\boldsymbol{F}_{int}$ depends nonlinearly on the deformation history and strain rate, and accounts for material plasticity, contact, and geometric nonlinearities. The external force vector $\boldsymbol{F}_{\text{ext}}$ includes the contact forces between colliding components and any prescribed boundary conditions.

An explicit central-difference scheme is employed to integrate Equation (4) in time. At time step n, the acceleration is computed as:

$$\ddot{\boldsymbol{u}}^n = \boldsymbol{M}^{-1}(\boldsymbol{F}_{ext}^n - \boldsymbol{F}_{int}^n) \tag{5}$$

where the superscript n denotes the time step index. The nodal velocities and displacements are updated using the standard staggered central difference formulas. The velocity update at the half time step is given by:

$$\dot{\boldsymbol{u}}^{n+\frac{1}{2}} = \dot{\boldsymbol{u}}^{n-\frac{1}{2}} + \Delta t \cdot \ddot{\boldsymbol{u}}^n \tag{6}$$

and the displacement update is:

$$\boldsymbol{u}^{n+1} = \boldsymbol{u}^n + \Delta t \cdot \dot{\boldsymbol{u}}^{n+\frac{1}{2}} \tag{7}$$

where Δt is the time step size, chosen to satisfy the Courant–Friedrichs–Lewy stability condition for the explicit scheme.

At the end of the simulation, the residual deformation of the carbody structures is extracted at the selected measurement points and used in the damage metric for the inverse reconstruction.

2.3. Surrogate-Based Inverse Optimization

2.3.1. Design of Experiments

Directly solving the inverse problem by repeatedly running the nonlinear dynamic FE model for many candidate parameter vectors $\boldsymbol{\theta}$ would be computationally prohibitive. To overcome this limitation, a surrogate model is constructed to approximate the mapping between $\boldsymbol{\theta}$ and the objective function value $\delta(\boldsymbol{\theta})$.

To generate training data for the surrogate, an Optimal Latin Hypercube Design (Opt LHD) [29,30] is used to sample the parameter space efficiently within the specified bounds. Let $\mathcal{X}$ denote the set of m sampled parameter vectors:

$$\chi = \left\{ \boldsymbol{\theta}^{(1)},\ \boldsymbol{\theta}^{(2)},\ \ldots,\ \boldsymbol{\theta}^{(m)} \right\} \tag{8}$$

where $\boldsymbol{\theta}^{(k)}$ is the k-th sample generated by the Opt LHD. For each design point $\boldsymbol{\theta}^{(k)}$, a nonlinear FE simulation is performed to compute the corresponding value of the objective function:

$$\boldsymbol{y}^{(k)} = \delta(\boldsymbol{\theta}^{(k)}), k = 1,\ 2,\ \ldots,\ m \tag{9}$$

2.3.2. Surrogate Model Construction

Kriging is chosen due to its ability to capture complex, nonlinear relationships with relatively few samples. Compared to other surrogate models, such as polynomial regression, Kriging often yields lower approximation error and better represents highly nonlinear functions—especially when data points are expensive to evaluate—making it suitable for accident reconstruction problems where sample efficiency is critical [31–33]. In Kriging, the response at any point $\boldsymbol{\theta}$ is modeled as the sum of a deterministic global trend and a zero-mean stochastic process:

$$\hat{\delta}(\boldsymbol{\theta}) = \mu + Z(\boldsymbol{\theta}) \tag{10}$$

where μ is a constant representing the global mean, and $Z(\boldsymbol{\theta})$ is a stationary Gaussian process with zero mean and variance σ^2. The covariance structure of $Z(\boldsymbol{\theta})$ is specified through a correlation function:

$$COV\left[Z(\boldsymbol{\theta}^{(i)}), Z(\boldsymbol{\theta}^{(j)})\right] = \sigma^2 R\left(\boldsymbol{\theta}^{(i)}, \boldsymbol{\theta}^{(j)}\right) \tag{11}$$

where $R(\boldsymbol{\theta}^{(i)}, \boldsymbol{\theta}^{(j)})$ is the correlation coefficient between the responses at $\boldsymbol{\theta}^{(i)}$ and $\boldsymbol{\theta}^{(j)}$. Typical choices include Gaussian, exponential, or Matérn correlation kernels, with hyperparameters estimated from the training data.

Let $\boldsymbol{y} = \left[y^{(1)}, y^{(2)}, \ldots, y^{(m)}\right]^{\mathrm{T}}$ be the vector of training responses, and let $\boldsymbol{R}$ be the $m \times m$ correlation matrix with entries $R_{ij} = R\left(\boldsymbol{\theta}^{(i)}, \boldsymbol{\theta}^{(j)}\right)$. The correlation vector between a prediction point $\boldsymbol{\theta}$ and the training points is denoted by $\boldsymbol{r}(\boldsymbol{\theta})$, with components $\boldsymbol{r}_j(\boldsymbol{\theta}) = R\left(\boldsymbol{\theta}, \boldsymbol{\theta}^{(i)}\right)$. Using ordinary Kriging, the estimated global mean $\hat{\mu}$ and the predicted response $\hat{\delta}(\boldsymbol{\theta})$ are given by:

$$\hat{\mu} = \frac{\mathbf{1}^T \boldsymbol{R}^{-1} \mathbf{y}}{\mathbf{1}^T \boldsymbol{R}^{-1} \mathbf{1}}, \ \hat{\boldsymbol{Y}}(\boldsymbol{x}) = \hat{\mu} + \boldsymbol{r}^T(\boldsymbol{\theta}) \boldsymbol{R}^{-1} (\boldsymbol{y} - \mathbf{1}\hat{\mu}) \tag{12}$$

where $\mathbf{1}$ is an m-dimensional vector of ones.

The associated Kriging mean squared error (MSE), which quantifies the prediction uncertainty, is expressed as:

$$s^2(\boldsymbol{\theta}) = \hat{\sigma}^2 [1 - \boldsymbol{r}^T(\boldsymbol{\theta}) \boldsymbol{R}^{-1} \boldsymbol{r}(\boldsymbol{\theta}) + \frac{\left(1 - \mathbf{1}^T \boldsymbol{R}^{-1} \boldsymbol{r}(\boldsymbol{\theta})\right)^2}{\mathbf{1}^T \boldsymbol{R}^{-1} \mathbf{1}}] \tag{13}$$

where $\hat{\sigma}^2$ is the estimated process variance. The Kriging surrogate $\hat{\delta}(\boldsymbol{\theta})$ is then used in place of the expensive FE model to approximate the objective function in the subsequent optimization.

2.3.3. Simulated Annealing Optimization

To search for the global minimum of the surrogate-based objective function and avoid being trapped in local minimum, a simulated annealing (SA) algorithm is adopted. SA is attractive in this context because it is simple to implement, has a modest number of tuning parameters, and can escape local minima when the surrogate landscape is nonlinear.

In SA, the optimization process is interpreted as the stochastic evolution of a Markov chain over the state space defined by $\boldsymbol{\theta}$. At a given temperature T, the transition probability from state $\boldsymbol{\theta}^{(i)}$ to state $\boldsymbol{\theta}^{(j)}$ is:

$$P(\boldsymbol{\theta}^{(i)} \to \boldsymbol{\theta}^{(j)}) = g(\boldsymbol{\theta}^{(i)}, \boldsymbol{\theta}^{(j)}) a(\boldsymbol{\theta}^{(i)}, \boldsymbol{\theta}^{(j)}) \tag{14}$$

where $g(\cdot, \cdot)$ is the generation probability of proposing state $\boldsymbol{\theta}^{(j)}$ from state $\boldsymbol{\theta}^{(i)}$, $\alpha(\cdot, \cdot)$ is the acceptance probability for moving from $\boldsymbol{\theta}^{(i)}$ to $\boldsymbol{\theta}^{(j)}$.

The probability of remaining in the current state $\boldsymbol{\theta}^{(i)}$ is then

$$P(\boldsymbol{\theta}^{(i)} \to \boldsymbol{\theta}^{(j)}) = 1 - \sum_{\boldsymbol{\theta}^{(j)} \in N(\boldsymbol{\theta}^{(i)})} P(\boldsymbol{\theta}^{(i)} \to \boldsymbol{\theta}^{(j)}) \tag{15}$$

where $N\left(\boldsymbol{\theta}^{(i)}\right)$ denotes the neighborhood of state $\boldsymbol{\theta}^{(i)}$. ensuring that the transition probabilities out of $\boldsymbol{\theta}^{(i)}$ sum to one.

The acceptance probability α is defined according to the Metropolis criterion. Let $\boldsymbol{E}^{(i)} = \hat{\delta}\left(\boldsymbol{\theta}^{(i)}\right)$ and $\boldsymbol{E}^{(j)} = \hat{\delta}\left(\boldsymbol{\theta}^{(j)}\right)$ be the objective function values associated with states $\boldsymbol{\theta}^{(i)}$ and $\boldsymbol{\theta}^{(j)}$, and define the energy difference $\Delta E = \boldsymbol{E}^{(i)} - \boldsymbol{E}^{(j)}$. The acceptance probability is

$$a(\boldsymbol{\theta}^{(i)}, \boldsymbol{\theta}^{(j)}) = \min\{1, \exp(\frac{-\Delta E}{T})\} \tag{16}$$

If $\Delta E \leq 0$, the move is always accepted, as it leads to a lower or equal objective function value. If $\Delta E > 0$, the move is accepted with probability $\exp(-\Delta E/T)$, allowing occasional uphill steps that help escape local minima. The temperature T is gradually decreased according to a prescribed cooling schedule, reducing the probability of accepting worse solutions as the search progresses. The algorithm stops when the temperature and the change in the objective function both fall below given thresholds, and annealing process is repeated until convergence criteria are met, yielding the optimal parameter set $\boldsymbol{\theta}^*$ that reconstructs the train collision scenario.

3. Case Study: Reconstruction of a High-Speed EMU Rear-End Collision

In this section, the methodology presented in Section 2 is applied to a real rear-end collision accident involving a high-speed Electric Multiple Unit (EMU) trainset. The objective is to reconstruct the pre-impact kinematic state of the vehicles from the observed residual damage of the carbody end structure.

3.1. Accident Description and Damage Characterization

3.1.1. Accident Overview

The case examined in this study is a rear-end collision between two EMU trainsets operating on a high-speed railway line. During operation, the trailing train impacted the preceding train, resulting in substantial damage localized near the inter-vehicle interface, while no pronounced global dynamic instabilities, such as derailment, climbing, or rollover, were observed. This accident therefore satisfies the key assumptions of the proposed method, in which the dominant information for reconstruction is provided by local end-structure deformation rather than by global vehicle-level dynamic instabilities.

For reconstruction, one end of a carbody that suffered the most pronounced structural damage is selected as the primary object of analysis, as shown in Figure 5. The damage pattern on this end wall provides crucial information for inferring the pre-impact relative position, orientation, and velocity of the colliding vehicles.

3.1.2. Residual Deformation Zones and Measurement Points

Based on detailed on-site inspection and photographic documentation, the residual deformation at the selected carbody end is mainly distributed in the following regions:

(1) Right-hand end wall near the doorway: pronounced inward indentation with maximum deformation approximately at mid-height of the door panel;
(2) Upper end wall region: only minor deformation, indicating limited vertical distortion of the end structure;
(3) Inner windshield mounting area: uniform inward deflection of the mounting seat and adjacent panel;
(4) Underframe–end wall junction: severe deformation and local tearing at the connection between the underframe and the end wall, implying large plastic strains and local failure;
(5) Lower left end wall region and left-hand doorway: inward bending with clear plate wrinkling, and severe bending and tearing of the left-hand door panel and its supporting members;

(6) Window region: essentially undeformed, so the window midpoint is adopted as a reference point for residual deformation measurements in the surrounding regions.

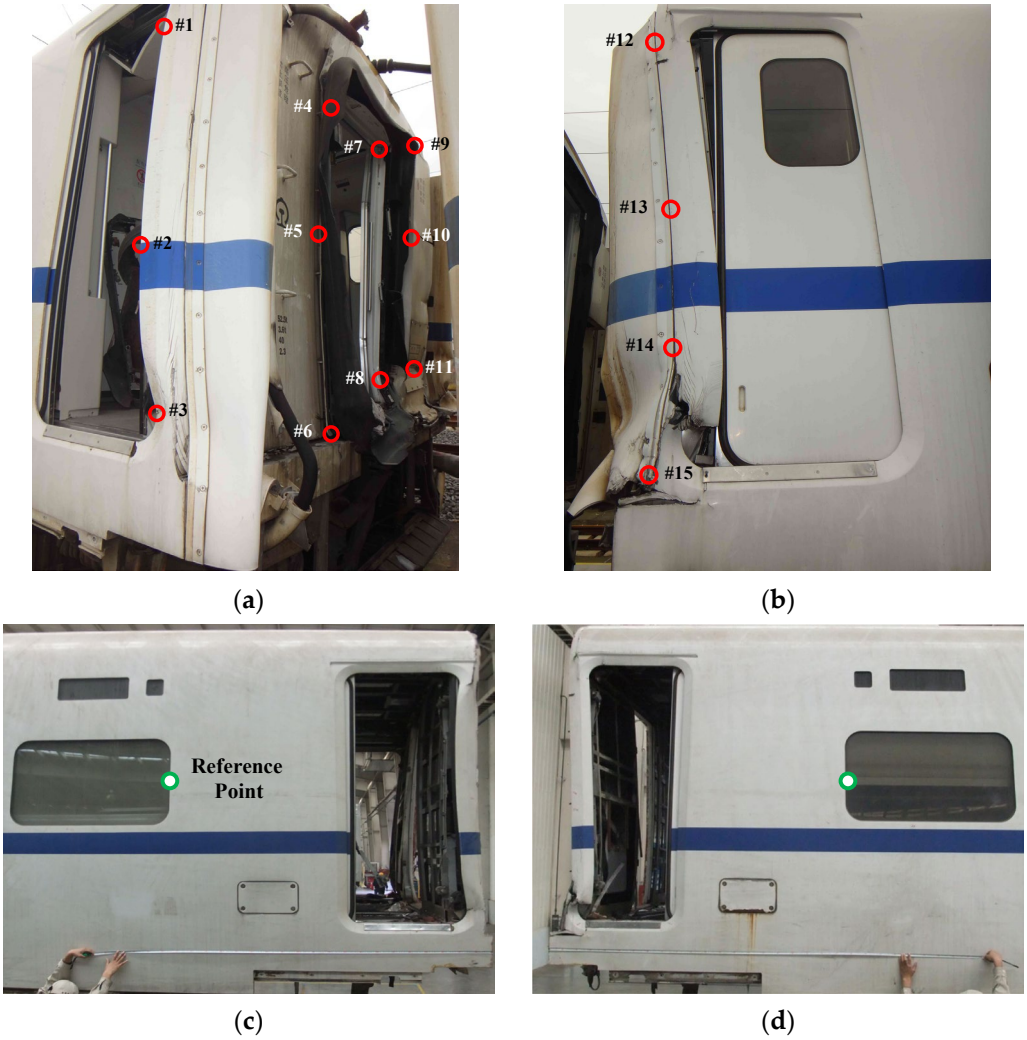


Figure 5. Layout of measurement and reference points for damage quantification (**a**) Measurement points in the front car; (**b**) Measurement points in the rear car; (**c**) Reference points in the front car; (**d**) Reference points in the rear car.

To quantitatively describe the residual damage pattern, measurement and reference points were defined on the damaged end structure. Specifically, 15 measurement points were placed within the major deformation zones identified from the on-site inspection to capture the spatial deformation pattern. Two reference points were selected in essentially undeformed regions; since the window area remained nearly intact after the collision, a location near the window-frame midpoint was used as the primary reference. The residual deformation data were obtained through on-site manual measurements conducted after the collision. Depending on site conditions and accessibility, measuring tapes and laser distance meters were used. For each measurement point, the residual deformation was defined as the relative distance between the measurement point and the reference point in the window-frame region. The measured residual displacements are summarized in Table 1.

Table 1. Measured distances from measuring points to reference points.

Point Number	Distance [mm]
1	1870
2	1820
3	1905
4	1965
5	1945
6	1990
7	1965
8	1925
9	2085
10	2035
11	1925
12	2020
13	1985
14	1975
15	2005

3.2. Case-Specific Inverse Problem Setup

3.2.1. Definition of Kinematic State Variables and Bounds

The observed damage pattern provides qualitative insight into the likely range of these parameters. For example, the concentration of damage near the right-hand side doorway and the tearing at the underframe–end wall junction suggests a non-zero lateral offset and yaw angle between the vehicles at impact. Similarly, the relatively small deformation at the top of the end wall and the preservation of the window frame constrain the possible roll and pitch angles. Based on such considerations, together with operational constraints (track geometry, clearance envelope, and speed limits), lower and upper bounds for each component of $\boldsymbol{\theta}$ are determined. These bounds are summarized in Table 2 and define the feasible region of the inverse problem.

Table 2. Variation ranges for the vehicle kinematic state parameters.

Variable	T_Y [mm]	T_Z [mm]	R_X [°]	R_Y [°]	R_Z [°]	V [m/s]
Range	[−200, 200]	[−200, 200]	[−2.5, 2.5]	[−2.5, 2.5]	[−2.5, 2.5]	[2, 10]

3.2.2. Objective Function and Optimization Problem

To quantify the similarity between the numerical and experimental damage patterns, the SSRD defined in Equation (1) is adopted as the objective function. Within the feasible parameter ranges given in Table 2, the goal is to find the vector $\boldsymbol{\theta}$ that minimizes the SSRD and thus best reproduces the measured residual deformation field. The mathematical structure of the optimization problem is identical to that in Equation (3).

$$\begin{aligned} \underset{\boldsymbol{\theta}}{\textit{minimize}} \quad & \delta(\boldsymbol{\theta}) = \sum_{i=1}^{15} \left(\frac{d_{is}(\boldsymbol{\theta}) - d_{im}}{d_{im}} \right)^2 \\ \textit{subject to} \quad & \boldsymbol{\theta} = \begin{bmatrix} T_Y & T_Z & R_X & R_Y & R_Z & V \end{bmatrix}^{\mathrm{T}} \\ & T_Y, T_Z \in [-200\ \mathrm{mm},\ 200\ \mathrm{mm}] \\ & R_X, R_Y, R_Z \in [-2.5\ ^\circ,\ 2.5\ ^\circ] \\ & V \in [2\ \mathrm{m/s},\ 10\ \mathrm{m/s}] \end{aligned} \tag{17}$$

3.3. FE Model of the Two-Vehicle Impact Unit

HyperMesh v2022.1 is used to construct the FE model, and LS-DYNA R13 is employed as the explicit dynamics solver. Figure 6 shows the FE model of a single vehicle, including

the side view, top view, side wall and roof, and underframe configuration. The underframe of the accident vehicle comprises side sills, cross beams, end beams, bolster beams and traction beams. These members are modelled explicitly using shell elements with thicknesses taken from the design drawings. The roof and side walls are represented by shell elements corresponding to the large hollow aluminum extrusions of the actual carbody.

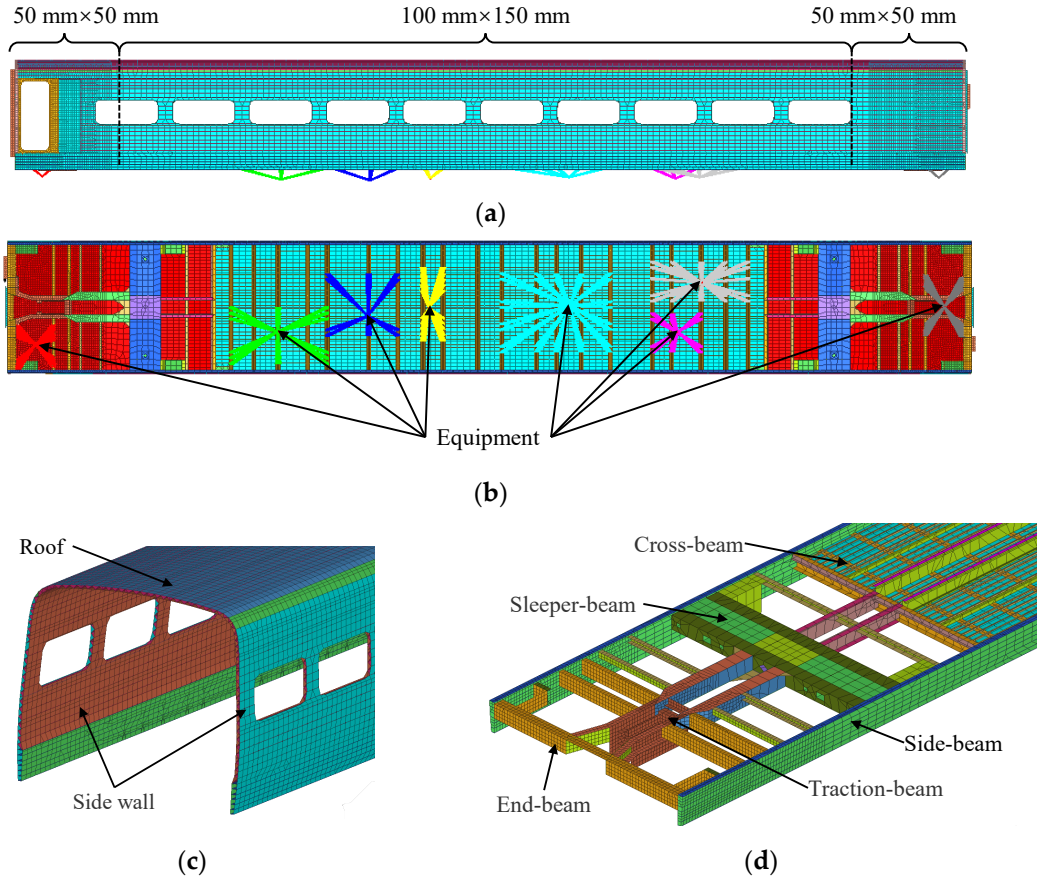


Figure 6. FE model of a single vehicle structure: (**a**) Side view; (**b**) Top view; (**c**) Sidewall and roof; (**d**) Underframe.

The vehicle end structures, which form the primary contact region and exhibit severe deformation in the accident, are discretized with finer elements of approximately 50 mm × 50 mm. The central regions of the carbody, which mainly experience elastic or mild plastic deformation, are meshed with typical element sizes of about 10 mm × 150 mm. Underfloor equipment and other auxiliary components with limited influence on the global stiffness are not modelled in geometric detail. Instead, they are represented by concentrated mass points. This results in a final two-vehicle model containing 293,838 elements and 212,826 nodes.

The carbody of the high-speed train is primarily composed of thin-walled aluminum-alloy structures. These are modelled using two-point integrated Belytschko–Tsay shell elements with shell thicknesses defined according to the structural drawings. The MAT_024 material model (piecewise linear isotropic plasticity) is adopted to describe the elastoplastic behavior under dynamic loading. A strain-based failure criterion is introduced so that elements exceeding the specified failure strain can fail, enabling realistic simulation of tearing and fracture during the collision process. The specific material parameters are listed in Table 3.

Table 3. Material properties of the aluminium alloy carbody structure used in the FE model.

Parameter	Value	
	Side Wall, End Wall, Roof	**Underframe**
Density [kg/m^3]	2700	2700
Tensile modulus [MPa]	69,000	69,000
Poisson's ratio [/]	0.3	0.3
Yield limit [MPa]	205	344
Strength limit [MPa]	245	465
Failure strain [/]	0.137	0.241

Automatic single-surface contact is defined for both vehicles to capture self-contact and mutual contact between their deforming structures. Hourglass control is applied to the under-integrated shell elements to suppress non-physical zero-energy modes during the high-speed impact. The two-vehicle impact model is assembled by placing the front end of the trailing car opposite the rear end of the leading car, as shown in Figure 7. One end of the stationary vehicle is constrained to a rigid wall to represent the restraint from the remaining trainset. All nodes of the moving vehicle are grouped and assigned an initial longitudinal velocity, which corresponds to the relative impact speed V in the kinematic parameter vector used for the inverse reconstruction.

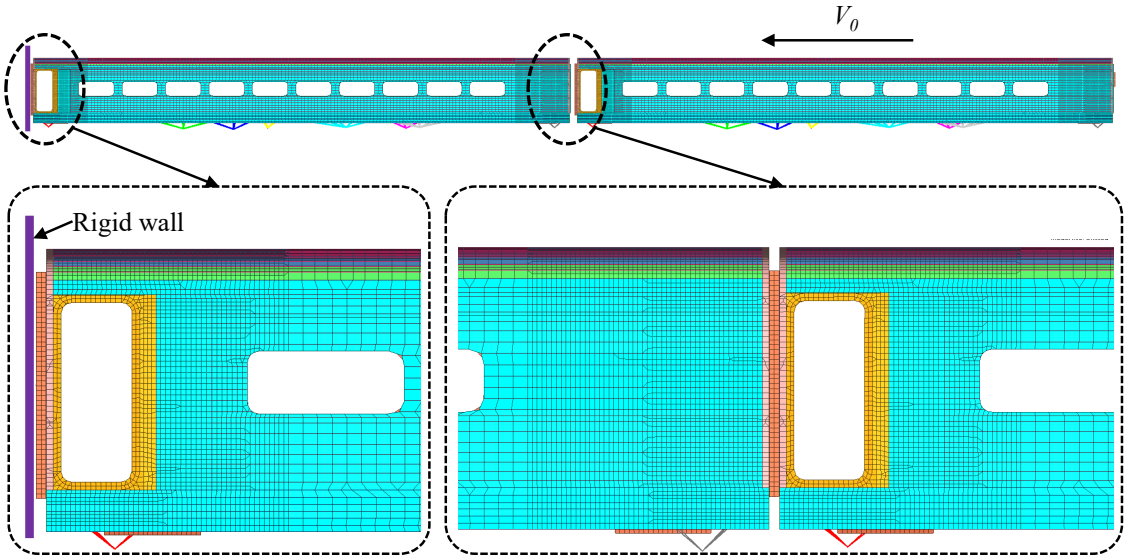


Figure 7. Schematic illustration of the two-vehicle impact configuration used in the FE simulations.

3.4. Surrogate Model Construction and Validation

In this study, the design of experiments, surrogate model construction, and optimization procedures are implemented in HyperStudy v2022.1.

3.4.1. Experimental Design and FE Simulations

For the experimental design, 100 sample points are generated using the Opt LHD method within the bounds. For each sample, a nonlinear FE simulation is performed and the corresponding SSRD value is computed. After excluding one invalid sample point, the remaining sample points are partially listed in Table 4.

Table 4. A subset of the DoE sample points generated by the Opt LHD method.

No.	T_Y [mm]	T_Z [mm]	R_X [°]	R_Y [°]	R_Z [°]	V [m/s]
1	−78.8	−54.6	−0.7	−1.7	2.4	−4.8
2	183.8	175.8	0.7	1.5	−0.8	−7.1
3	196.0	26.3	1.6	0.3	1.2	−6.7
4	−54.6	183.8	1.0	1.2	−1.9	−7.2
5	−123.2	−103.0	1.8	−2.0	−0.1	−8.7
6	22.2	−2.0	−1.6	−2.2	−2.2	−5.7
7	−196.0	66.7	0.6	2.1	−1.4	−4.4
8	−14.1	−34.3	−0.1	2.5	1.3	−3.9
9	123.2	−62.6	−1.9	−1.1	2.1	−7.7
10	163.6	−14.1	0.8	−2.5	0.4	−7.5
11	143.4	34.3	0.8	2.4	−2.1	−3.9
⋮	⋮	⋮	⋮	⋮	⋮	⋮
96	−18.2	−38.4	−0.6	2.4	−2.0	−7.3
97	−70.7	139.4	−1.0	0.1	2.5	−6.9
98	179.8	−143.4	−1.4	−1.5	−0.5	−5.6
99	−86.9	−99.0	−0.4	−1.9	−1.2	−2.2

3.4.2. Kriging Accuracy and Response Surface Behavior

Based on the training dataset, a Kriging model is constructed to approximate the objective function $\delta(\boldsymbol{\theta})$. The constant regression function serves as a simple and robust model for the global trend, while the Gaussian correlation function is adopted to provide smooth interpolation. The correlation hyperparameters are estimated via maximum likelihood estimation during training. To assess its predictive performance, the design points are divided into training and validation sets. A set of 30 validation samples is randomly selected for error analysis, as illustrated in Figure 8.

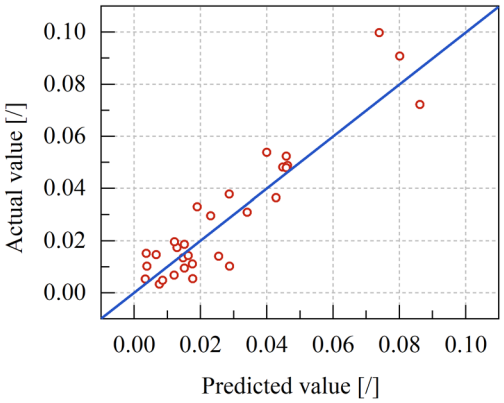


Figure 8. Accuracy assessment of the constructed Kriging surrogate model.

The Kriging predictions $\hat{\delta}(\boldsymbol{\theta})$ are then compared with the true FE-based values $\delta(\boldsymbol{\theta})$ using the coefficient of determination R^2 [34]. The Kriging model exhibits good agreement with the FE results, yielding $R^2 = 0.85$. This indicates a strong positive correlation between predicted and true values and confirms that the surrogate provides sufficient accuracy over the region of interest. Once validated, the Kriging surrogate is adopted as the objective function in place of the original FE model for subsequent global optimization.

Figure 9 shows representative two-dimensional sections of the surrogate-predicted objective function as a function of each pair of kinematic parameters, while keeping the remaining parameters fixed at their nominal values.

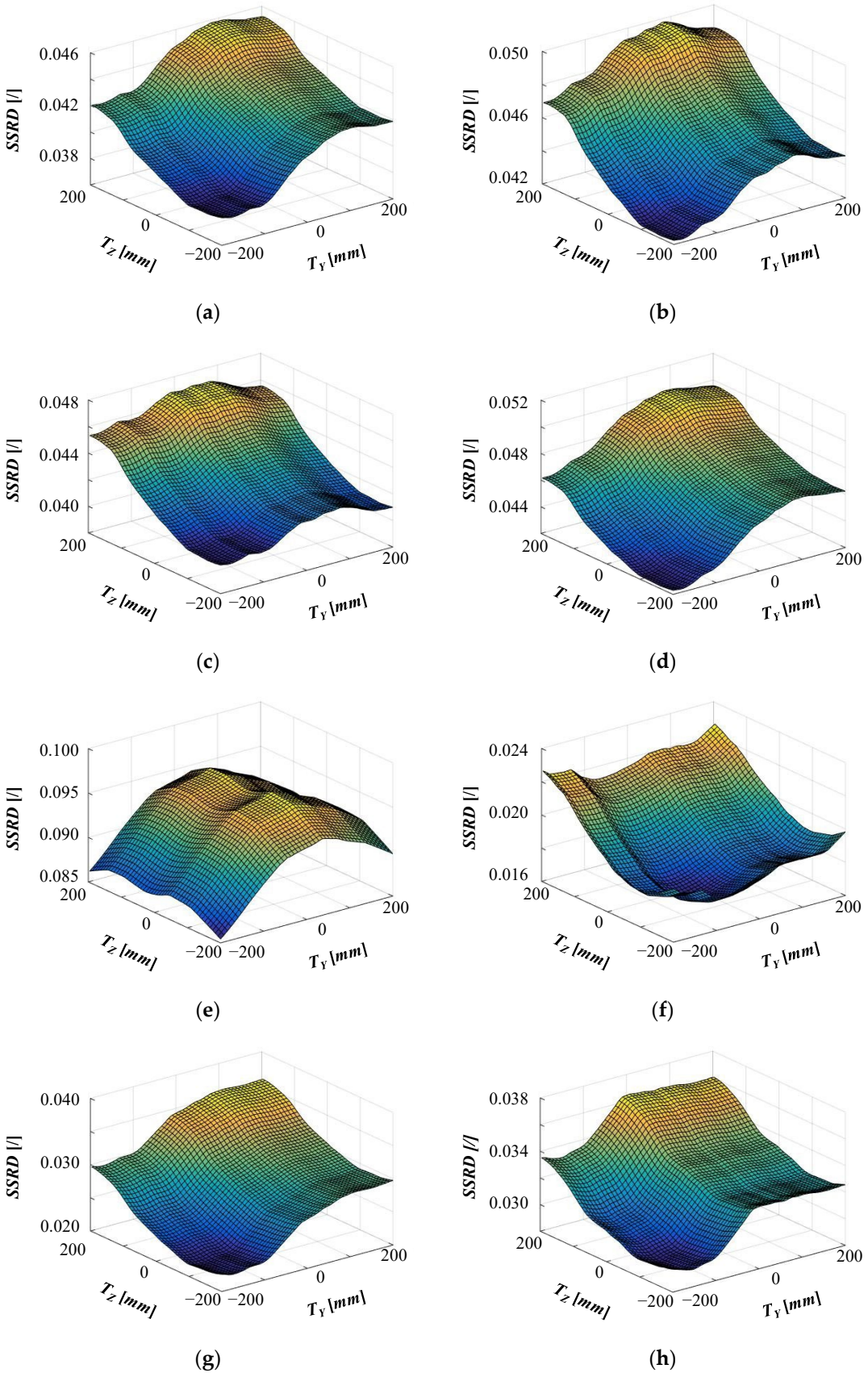


Figure 9. Representative response surfaces of the Kriging model: (**a**) $R_X = -2.5°$, $R_Y = 0$, $R_Z = 0°$, $V = 2$ m/s; (**b**) $R_X = 2.5°$, $R_Y = 0°$, $R_Z = 0°$, $V = 2$ m/s; (**c**) $R_X = 0°$, $R_Y = -2.5°$, $R_Z = 0°$, $V = 2$ m/s; (**d**) $R_X = 0°$, $R_Y = 2.5°$, $R_Z = 0°$, $V = 2$ m/s; (**e**) $R_X = 0°$, $R_Y = 0°$, $R_Z = -2.5°$, $V = 2$ m/s; (**f**) $R_X = 0°$, $R_Y = 0°$, $R_Z = 2.5°$, $V = 2$ m/s; (**g**) $R_X = 0°$, $R_Y = 0°$, $R_Z = 0°$, $V = 5$ m/s; (**h**) $R_X = 0°$, $R_Y = 0°$, $R_Z = 0°$, $V = 10$ m/s.

Overall, the response surfaces exhibit a well-defined valley region rather than a highly fragmented multi-peak landscape. Within the prescribed bounds of $\boldsymbol{\theta}$, moving away from this valley in any parameter direction leads to a clear increase in SSRD. This indicates that, under the current data and parameter ranges, the inverse problem is numerically well-posed in the sense that there exists a distinct region of low objective function values corresponding to plausible collision scenarios.

The response surfaces also reveal distinct differences in sensitivity among the six kinematic parameters $(T_Y, T_Z, R_X, R_Y, R_Z, V)$. Variations in the vertical offset T_Z and the impact velocity V produce relatively steep gradients in the objective function, indicating that the residual damage pattern is highly sensitive to changes in these parameters. In contrast, the surfaces are noticeably flatter with respect to lateral offset T_Y and, to a lesser extent, certain rotational parameters, particularly R_X. This implies that T_Z and V are more strongly constrained by the available damage measurements and can be identified with higher confidence.

These observations justify the use of a global optimization algorithm such as simulated annealing. The nonlinearity and parameter interactions evident in Figure 9 make purely local gradient-based methods vulnerable to premature convergence or failure to follow the valley structure in the high-dimensional space. By allowing occasional uphill moves and exploring the parameter space more broadly, simulated annealing is better suited to track the elongated low-SSRD regions and to locate the global minimum on the surrogate landscape.

3.5. Optimization Results and Reconstructed Collision Scenario

The SA algorithm is employed to solve the optimization problem. After 10,000 iterations, an optimal set of parameters and the corresponding minimum SSRD value are obtained, as presented in Table 5.

Table 5. Optimized parameters and the corresponding minimum objective function value obtained by the SA algorithm.

Variable	T_Y [mm]	T_Z [mm]	R_X [°]	R_Y [°]	R_Z [°]	V [m/s]	*SSRD* [/]
Value	0.0	−137.2	0.0	0.6	−0.3	−4.0	0.027

The optimized parameters were reintegrated into the FE model to simulate the structural damage of the vehicles involved in the accident, as depicted in Figure 10. The simulation outcomes were then compared with the actual accident data, encompassing both visual and numerical comparisons.

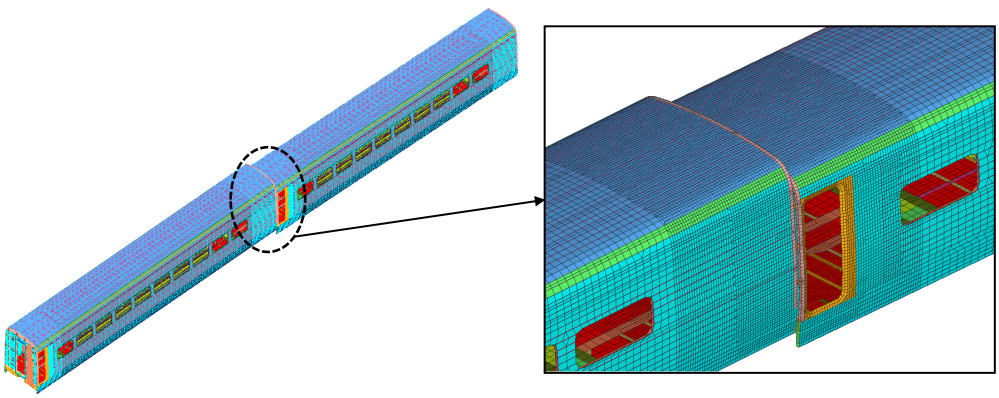


Figure 10. Optimized initial collision configuration.

4. Results and Discussion

4.1. Comparison Between Simulated and Observed Structural Damage

To evaluate the quality of the reconstruction, the structural damage predicted by the FE simulation using the optimized parameters was compared with the actual accident observations.

Figure 11 compares the damage pattern from the FE model with photographs from the accident site. The comparison shows a high level of qualitative agreement. The severe deformation at the junction between the underframe and the end wall, including associated tearing, is well captured. The inward indentation of the right-hand doorway and the wrinkling of the lower left end wall panel are also reproduced in both location and mode. In addition, the relatively small deformation at the top of the end wall and the preservation of the window frame are consistent between simulation and observation, indicating that the global distortion of the end structure is correctly represented.

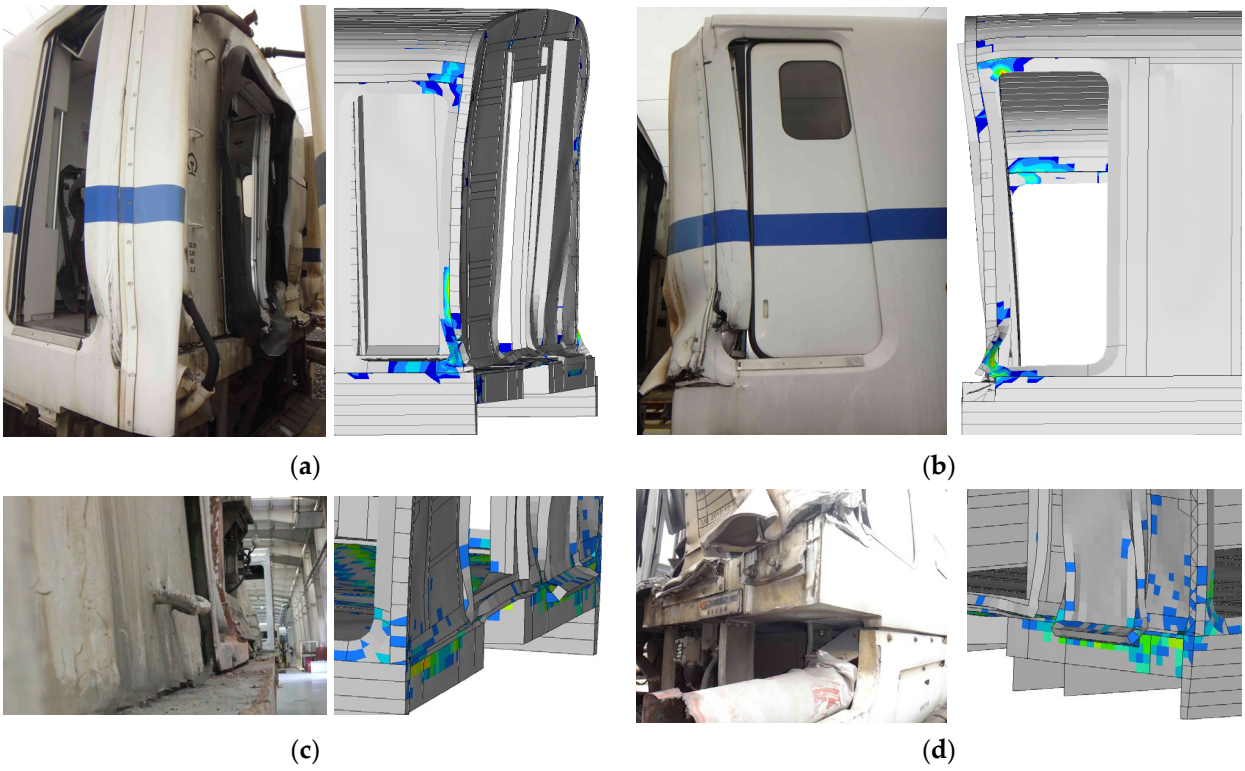


Figure 11. The damage result comparison between accident photograph and FE model: (**a**) Global deformation of the front car end structure; (**b**) Global deformation of the rear car end structure; (**c**) Local deformation features of the front car end structure; (**d**) Local deformation features of the rear car end structure.

Table 6 provides a quantitative assessment of the residual deformation at 15 key measurement points. For each point, the distance to the reference point obtained from the reconstructed FE model is compared with the value extracted from accident photographs. For most points, the relative error between the simulation and the measurement is below approximately 5%, whereas a few points exhibit larger discrepancies, with a maximum value of 8.9%. Overall, the larger discrepancies tend to occur in regions with severe localized deformation, such as wrinkling or tearing, as well as near structural discontinuities, such as the door-frame boundaries. These locations are generally more sensitive to measurement uncertainty because point identification is more difficult on irregularly deformed surfaces. They are also more affected by modelling idealizations, since simplified local

details can have a stronger influence on local deformation modes. Taken together, the qualitative comparison with photographs and the quantitative error metrics indicate that the optimized kinematic state, together with the reduced two-vehicle FE model, provides a reliable reconstruction of the collision for structural damage analysis and subsequent safety interpretation.

Table 6. Comparison between simulation-predicted and actual measured deformation at key points.

Point Number	Measured [mm]	Simulated [mm]	Relative Error [%]
1	1870	1910	2.1
2	1820	1918	5.4
3	1905	1929	1.3
4	1965	2031	3.4
5	1945	2031	4.4
6	1990	2068	3.9
7	1965	2028	3.2
8	1925	2025	5.2
9	2085	2129	2.1
10	2035	2072	1.8
11	1925	2097	8.9
12	1985	2069	4.2
13	1975	2075	5.1
14	2005	2087	4.1
15	2085	2129	2.1

4.2. Implications for Railway Safety and Accident Investigation

First, the case study demonstrates that detailed pre-impact kinematic conditions can be inferred from post-accident structural damage with engineering accuracy, even when only limited site measurements are available. In many real-world investigations, high-quality deformation records are more readily accessible than complete operational data. The present approach shows that such damage information can be used in a systematic and quantitative way to reconstruct key impact parameters, rather than serving only as qualitative evidence.

Second, the framework provides a structured way to incorporate advanced numerical models into accident investigation without incurring prohibitive computational cost. By combining a reduced two-vehicle FE model with a Kriging surrogate and a global optimization algorithm, the method retains the essential realism of nonlinear FE crash simulation while enabling efficient exploration of the kinematic parameter space. This is particularly relevant for railway administrations and safety authorities, who often face tight time constraints in major accident investigations. In such contexts, the ability to generate a physically consistent reconstruction within manageable computational effort can support decision-making on urgent issues, such as verifying assumed collision scenarios or assessing the robustness of preliminary findings.

Third, the sensitivity and correlation patterns revealed by the surrogate model highlight where additional data would most effectively reduce reconstruction uncertainty. Parameters such as vertical offset and impact velocity, to which the damage metric is highly sensitive, can be estimated with relatively narrow confidence intervals from structural deformation alone. In contrast, parameters that lie along correlated directions, such as lateral offset and certain rotations, are less well constrained and may require external information—such as on-board recorder data, track geometry surveys or post-accident vehicle attitude measurements—to be uniquely determined. This suggests a more targeted approach to evidence collection: site surveys and data retrieval efforts can be focused on observables that are most informative for resolving the ambiguities identified by the

reconstruction. Accordingly, accident investigations should prioritize evidence that constrains the highly sensitive parameters, particularly impact velocity and vertical offset, since these can be identified with higher confidence from structural deformation. Conversely, parameters that exhibit lower sensitivity or stronger correlation require complementary information, such as recorder data or track geometry, to reliably identify accident causes.

Finally, the methodological structure of the framework is sufficiently general to be extended beyond the specific EMU rear-end collision studied here. The same surrogate-assisted inverse analysis could, in principle, be applied to other rail impact scenarios, including level-crossing collisions, buffer-stop impacts, or multi-vehicle pile-ups, provided that appropriate FE models and damage measurements are available. These developments would further enhance the role of quantitative reconstruction methods in supporting evidence-based improvements to railway crashworthiness and accident prevention strategies.

5. Conclusions

This study proposed and applied a systematic surrogate-based inverse analysis framework for reconstructing structural damage in train collision accidents. The method combines FE modelling, Kriging surrogate modelling, and global optimization by simulated annealing to infer the pre-impact kinematic state from post-accident residual deformations. Based on the application to a real high-speed EMU rear-end collision, the main conclusions are as follows:

(1) A practical framework for train accident reconstruction was established. The damage-based inverse problem was formulated using an SSRD metric between measured and simulated residual deformations. A reduced two-vehicle FE model, coupled with a Kriging surrogate and simulated annealing, provides a computationally efficient approach suitable for systematic reconstruction studies of train collisions.

(2) The Kriging surrogate accurately reproduces the FE response in the relevant parameter space. Using an Optimal Latin Hypercube Design, the surrogate achieved good agreement with FE-computed SSRD values (coefficient of determination on the order of 0.85). The response surfaces in the plane are smooth and effectively unimodal, indicating that the surrogate preserves the essential nonlinear trends and is reliable for global optimization.

(3) The reconstructed kinematic state yields good agreement with observed structural damage. The optimal solution obtained by simulated annealing corresponds to a physically plausible impact configuration with modest yaw and pitch, a pronounced vertical offset, and a moderate relative impact velocity. When this state is applied in the FE model, the simulated damage pattern reproduces the main features observed on site, and the residual deformation at key measurement points is generally within a few percent of the measured values.

(4) Sensitivity and correlation analyses highlight which parameters are identifiable. The response surfaces show that the damage metric is more sensitive to vertical offset than to lateral offset, and that these two parameters exhibit noticeable correlation along valley-type regions of nearly constant SSRD. This implies that the reconstruction constrains some components of the kinematic state more tightly than others, and that a band of equivalent combinations may exist. Such insights are important when interpreting reconstruction results in accident investigations.

(5) The methodology has potential value for railway safety analysis and forensic investigation. By enabling quantitative reconstruction of train collisions with limited measurement data, the proposed approach can support root-cause analysis, assessment of crashworthiness improvements, and the development of digital twins for

rapid scenario replay. Its reliance on standard FE tools and generic surrogate-based optimization makes it transferable to other types of rail impact events.

Several limitations should be acknowledged. The reduced-order FE model involves simplifications of certain structural details and boundary conditions, which may influence local damage predictions. Measurement data are limited to a finite number of deformation points, and uncertainties in both measurements and material properties are not yet treated explicitly. Future work will therefore focus on (i) extending the framework to multi-collision scenarios, and (ii) integrating additional sources of information, such as on-board event recorder data and track geometry, to further improve the robustness and interpretability of accident reconstructions.

Author Contributions: H.Z.: Methodology, Visualization, Writing—review & editing; D.Z.: Software, Investigation; P.X.: Supervision. All authors have read and agreed to the published version of the manuscript.

Funding: This work was supported by the National Natural Science Foundation of China (No. 52302460), and the Zhejiang Provincial Natural Science Foundation of China (No. ZCLQN25E0502).

Data Availability Statement: The data are available upon reasonable request.

Acknowledgments: The authors are thankful to the National Nature Science Foundation of China (NSFC), the Science Technology Department of Zhejiang Province. The authors would like to acknowledge the support from the Key Laboratory of Rail Transit Safety of the Ministry of Education at Central South University for providing the experimental platform and technical assistance. The authors are grateful to the editors and the anonymous reviewers for their insightful comments and suggestions.

Conflicts of Interest: D.Z. from China Railway Guangzhou Group Co., Ltd., the remain author declares there is no conflict of interest.

References

1. Yao, S.; Kong, L.; Xu, P.; Xiao, X.; Peng, Y. Investigation on the Dynamic Characteristic of Occupant During the Frontal Collision Between High-Speed Train and Obstacle. *Accid. Anal. Prev.* **2024**, *199*, 107495. [CrossRef]
2. Deng, G.; Wang, F.; Yu, C.; Peng, Y.; Xu, H.; Li, Z.; Hou, L.; Wang, Z. Assessment of Standing Passenger Traumatic Brain Injury Caused by Ground Impact in Subway Collisions. *Accid. Anal. Prev.* **2022**, *166*, 106547. [CrossRef]
3. Zhu, T.; Xiao, S.; Lei, C.; Wang, X.; Zhang, J.; Yang, B.; Yang, G.; Li, Y. Rail Vehicle Crashworthiness Based on Collision Energy Management: An Overview. *Int. J. Rail Transp.* **2021**, *9*, 101–131. [CrossRef]
4. Zhou, Y.; Tao, X.; Luan, L.; Ning, J. Revisiting the 7/23 Train Accident Using Computer Reconstruction Simulation for Causation and Prevention Analysis. *Math. Comput. Simul.* **2018**, *148*, 1–15. [CrossRef]
5. Yang, C.; Li, Q.; Xiao, S.; Wang, X. On the Overriding Issue of Train Front End Collision in Rail Vehicle Dynamics. *Veh. Syst. Dyn.* **2018**, *56*, 506–528. [CrossRef]
6. Zhao, H.; Xu, P.; Jiang, S.; Li, B.; Yao, S.; Xing, J.; Huang, Q.; Xu, K. A Novel Design Method of the Impact Zone of a High-Speed Train. *Int. J. Crashworthiness* **2022**, *27*, 476–485. [CrossRef]
7. Zhu, T.; Liu, S.; Xiao, S.; Che, Q. Train Collision Dynamic Model Considering Longitudinal and Vertical Coupling. *Adv. Mech. Eng.* **2019**, *11*, 1–9. [CrossRef]
8. Zhang, W. Dynamic Modeling of Coupled Systems in the High-Speed Train. In *Dynamics of Coupled Systems in High-Speed Railways*; Zhang, W., Ed.; Elsevier: Amsterdam, The Netherlands, 2020; pp. 55–181.
9. Severson, K.J. Development of Collision Dynamics Models to Estimate the Results of Full-Scale Rail Vehicle Impact Tests. Master's Thesis, Tufts University, Medford, MA, USA, 2000.
10. Jacobsen, K.M. Collision Dynamics Modeling of Crash Energy Management Passenger Rail Equipment. Master's Thesis, Tufts University, Medford, MA, USA, 2008.
11. Liu, B.; Xu, Y.; Shi, H. Train Derailment Accident Simulation Based on ADAMS. *J. Comput. Appl.* **2010**, *30*, 174–176. (In Chinese)
12. Shi, H.; Xu, Y.; Liu, B. Train Accident Reconstruction System Based on Virtual Reality. *J. Comput. Appl.* **2010**, *30*, 177–179+229. (In Chinese)

13. Llana, P.; Tyrell, D. Preliminary Reconstruction of the November 30, 2007, Chicago, IL Rail Collision Available to Purchase. In Proceedings of the 2011 Joint Rail Conference, Pueblo, CO, USA, 16–18 March 2011. [CrossRef]
14. Wei, L.; Lian, H.; Yi, F. Simulation Research on Train Derailment and Colision Accident in Rban Rai Transit. *Urban Mass Transit* **2024**, *27*, 208–214. [CrossRef]
15. Santos, K.; Silva, N.M.; Dias, J.P.; Amado, C. A Methodology for Crash Investigation of Motorcycle-Cars Collisions Combining Accident Reconstruction, Finite Elements, and Experimental Tests. *Eng. Fail. Anal.* **2023**, *152*, 107505. [CrossRef]
16. Cao, Y.; Luo, Y. The Synthesized Method Based on Classical Mechanics and Finite Element for Vehicle Collision Accident Reconstruction Analysis. *Int. J. Crashworthiness* **2022**, *27*, 1790–1797. [CrossRef]
17. Vangi, D.; Gulino, M.-S.; Fiorentino, A.; Virga, A. Crash Momentum Index and Closing Velocity as Crash Severity Index. *Proc. Inst. Mech. Eng. Part D-J. Automob. Eng.* **2019**, *233*, 3318–3326. [CrossRef]
18. Gidlewski, M.; Prochowski, L.; Jemiol, L.; Zardecki, D. The Process of Front-to-Side Collision of Motor Vehicles in Terms of Energy Balance. *Nonlinear Dyn.* **2019**, *97*, 1877–1893. [CrossRef]
19. Baker, C.E.; Martin, P.; Montemeglio, A.; Li, R.; Wilson, M.; Sharp, D.J.; Ghajari, M. Inherent Uncertainty in Pedestrian Collision Reconstruction: How Evidence Variability Affects Head Kinematics and Injury Prediction. *Accid. Anal. Prev.* **2024**, *208*, 107726. [CrossRef]
20. Shang, S.; Masson, C.; Llari, M.; Py, M.; Ferrand, Q.; Arnoux, P.-J.; Simms, C. The Predictive Capacity of the MADYMO Ellipsoid Pedestrian Model for Pedestrian Ground Contact Kinematics and Injury Evaluation. *Accid. Anal. Prev.* **2021**, *149*, 105803. [CrossRef] [PubMed]
21. Santos, K.; Dias, J.P. Motorcycle Accident Reconstruction: Influence of Structural Deformation or Failure. *Eng. Fail. Anal.* **2020**, *115*, 104597. [CrossRef]
22. Li, Z.; Wu, H.; Xiao, Y.; Yu, C.; Lu, Y.; Li, J.; Cheng, W.; Jiang, X. An Aircraft Accident Reconstruction by Numerical Simulation Method and Investigations of Impact Force. *Eng. Fail. Anal.* **2022**, *142*, 106815. [CrossRef]
23. Liu, Y.; Wan, X.; Xu, W.; Shi, L.; Deng, G.; Bai, Z. An Intelligent Method for Accident Reconstruction Involving Car and E-Bike Coupling Automatic Simulation and Multi-Objective Optimizations. *Accid. Anal. Prev.* **2022**, *164*, 106476. [CrossRef] [PubMed]
24. Liu, Q.; Liu, J.; Wu, X.; Han, X.; Cao, L.; Guan, F. An Inverse Reconstruction Approach Considering Uncertainty and Correlation for Vehicle-Vehicle Collision Accidents. *Struct. Multidiscip. Optim.* **2019**, *60*, 681–698. [CrossRef]
25. Wang, X.; Peng, Y.; Yu, W.; Xie, P.; Zhang, H.; Hu, L.; Quan, Y. The Analyses of Vehicle-to-Pedestrian Accidents by Integrating Rigid-Body Simulation and Robust Optimization Techniques. *Int. J. Comput. Methods* **2020**, *17*, 1950026. [CrossRef]
26. Bruski, D.; Pachocki, L.; Sciegaj, A.; Witkowski, W. Speed Estimation of a Car at Impact with a W-Beam Guardrail Using Numerical Simulations and Machine Learning. *Adv. Eng. Softw.* **2023**, *184*, 103502. [CrossRef]
27. Seyedi, M.; Jung, S.; Wekezer, J. A Comprehensive Assessment of Bus Rollover Crashes: Integration of Multibody Dynamic and Finite Element Simulation Methods. *Int. J. Crashworthiness* **2022**, *27*, 273–288. [CrossRef]
28. Deng, G.; Peng, Y.; Hou, L.; Li, Z.; Li, B.; Yu, C.; Simms, C. A Novel Simplified FE Rail Vehicle Model in Longitudinal and Lateral Collisions. *Machines* **2022**, *10*, 1214. [CrossRef]
29. Liu, K.; Jing, L.; Wang, K.; Li, Q. Design Optimization of the Bamboo-Inspired Foam-Filled Tube for High-Speed Train Collision Energy Absorption. *Int. J. Mech. Sci.* **2024**, *271*, 109128. [CrossRef]
30. Wang, S.; Peng, Y.; Wang, T.; Che, Q.; Xu, P. Collision Performance and Multi-Objective Robust Optimization of a Combined Multi-Cell Thin-Walled Structure for High Speed Train. *Thin-Walled Struct.* **2019**, *135*, 341–355. [CrossRef]
31. Teng, D.; Feng, Y.-W.; Chen, J.-Y. Intelligent Moving Extremum Weighted Surrogate Modeling Framework for Dynamic Reliability Estimation of Complex Structures. *Eng. Fail. Anal.* **2022**, *138*, 106364. [CrossRef]
32. Jiang, Z.; Huang, X.; Chang, M.; Li, C.; Ge, Y. Thermal Error Prediction and Reliability Sensitivity Analysis of Motorized Spindle Based on Kriging Model. *Eng. Fail. Anal.* **2021**, *127*, 105558. [CrossRef]
33. Mukhtar, A.; Yasir, A.S.H.M.; Nasir, M.F.M. A Machine Learning-Based Comparative Analysis of Surrogate Models for Design Optimisation in Computational Fluid Dynamics. *Heliyon* **2023**, *9*, e18674. [CrossRef] [PubMed]
34. Narasinh, V.; Mital, P.; Chakravortty, N.; Mittal, S.; Kulkarni, N.; Venkatraman, C.; Rajakumar, A.G.; Banerjee, K. Investigating Power Loss in a Wind Turbine Using Real-Time Vibration Signature. *Eng. Fail. Anal.* **2024**, *159*, 108010. [CrossRef]

Disclaimer/Publisher's Note: The statements, opinions and data contained in all publications are solely those of the individual author(s) and contributor(s) and not of MDPI and/or the editor(s). MDPI and/or the editor(s) disclaim responsibility for any injury to people or property resulting from any ideas, methods, instructions or products referred to in the content.